Journal of the Optical Society of America B
OPTICAL PHYSICS

Plasmon optical trapping using silicon nitride trench waveguides

Qiancheng Zhao,[1] Caner Guclu,[1] Yuewang Huang,[1] Filippo Capolino,[1] Regina Ragan,[2] and Ozdal Boyraz[1,*]

[1]Department of Electrical Engineering and Computer Science, University of California, Irvine, California 92697, USA
[2]Department of Chemical Engineering and Material Science, University of California, Irvine, California 92697, USA
*Corresponding author: oboyraz@uci.edu

Received 22 February 2016; revised 16 April 2016; accepted 25 April 2016; posted 28 April 2016 (Doc. ID 259769); published 19 May 2016

We theoretically demonstrate optical trapping using a silicon nitride (Si_3N_4) trench waveguide on which bow-tie plasmonic nanoantennas are employed for enhancing optical forces. The electric field tailing away from the waveguide is transformed and then enhanced by the plasmonic nanoantennas deposited on the waveguide surface. We show that, with gold bow-tie nanoantennas, the waveguide system exhibits outstanding trapping capability on a 10 nm radius polystyrene nanoparticle, due to a 60-fold electric field enhancement in the proximity of the nanoantenna gap. This enhancement causes a boost of the optical trapping force by 3 orders of magnitude. The gradient force in the vertical direction is also calculated semi-analytically by using a dipole approximation of a scattering polystyrene nanosphere, and the analytical solution well matches the full-wave simulations. Mode polarization effects are discussed in this paper as a way to switch trapping. These investigations indicate that the patterned Si_3N_4 trench waveguide is suitable for optical trapping and nanoparticle sensing applications.

OCIS codes: (230.7370) Waveguides; (350.4855) Optical tweezers or optical manipulation; (250.5403) Plasmonics.

http://dx.doi.org/10.1364/JOSAB.33.001182

1. INTRODUCTION

Since the demonstration of optical manipulation on small objects exploited by Ashkin [1], there have been enormous improvements in optical tweezing, which has the ability to trap and transport particles from several micrometers to a few hundred nanometers [2–4]. Many researchers and commercial products in this field have focused on free-space laser beam trapping, which usually requires high-numerical-aperture lenses [5]. However, this high numerical aperture leads to a relatively narrow field of view and a very short focal length, which prevents continuous transportation of nanoparticles. Alternatively, a low numerical aperture can also be used in optical trapping [6]. This approach has been experimentally demonstrated by utilizing the interference patterns from multiple beams [6], two counterpropagating beams [1], and surface tension [7] to balance the axial scattering force. Nevertheless, no matter if it is with a high or low numerical aperture, these diffraction-limited systems have some fundamental drawbacks. To be specific, diffraction limits how tightly the beam can be focused, which affects the focal point intensity and intensity gradient and thereby limits the total trapping strength. Besides, the lens-involved system is usually bulky, which is incompatible with the integrated lab-on-chip platform. In an attempt to address these issues, waveguide-based near-field methods [8–11] have been developed in the past decade.

Due to the lack of beam foci, waveguide-based systems rely on the gradient force in evanescent fields [12]. The evanescent field partially polarizes the particle resulting in an extremely strong Lorenz force analogous to the trapping force in the traditional optical tweezers. However, these approaches suffer from the inefficient use of power because the evanescent field decays quickly outside the waveguide. This makes trapping particles smaller than 100 nm diameter difficult due to the weak light–matter interaction. To solve the problem, metallic structures are utilized to create local surface plasmons that enhance trapping strength [13,14]. The enhanced near-field method has been widely used in optical tweezing such as nanoparticle trapping [15], molecules sensing [13], bio cell control [16], and particle transportation [17–19]. The use of an integrated planar waveguide for optical tweezing is often combined with an optofluidic [20–22] to deliver particles. However, extra steps must be implemented to build microfluidic channels for these hybrid integrated plasmonic–photonic waveguides [23,24]. Recently, a novel approach of an Si_3N_4 trench waveguide has been put forward by our group with the capability to combine microfluidic channels and waveguides together [25,26]. In the method proposed here, analyte contained in the trapezoidal trench interacts

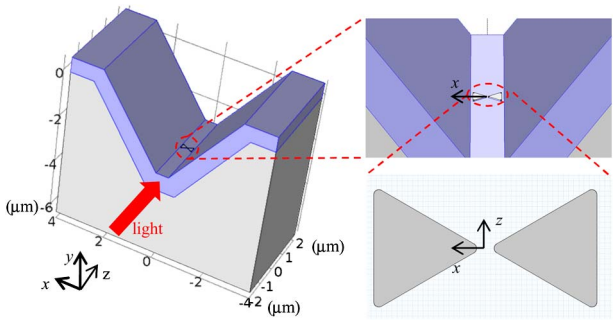

Fig. 1. Schematic illustration of the proposed Si_3N_4 trench waveguide with a bow-tie antenna for optical trapping. The gray-colored region is the SiO_2 substrate, and the blue-colored V-shaped volume is the Si_3N_4 guiding layer. The top cladding region is assumed to be water; it is not shown in the figure in order to permit the bow-tie antenna to be visible. The bow-tie antenna is located in the trench valley, sitting on top of the Si_3N_4 layer.

with the field tailing away from the trench waveguide, which can be enhanced by a plasmonic bow-tie antenna, as shown in Fig. 1.

In this paper, we theoretically propose and analytically verify a near-field optical trapping design utilizing a Si_3N_4 trench waveguide with bow-tie antennas for field enhancement [27], as shown in Fig. 1. The bow-tie antenna leads to a 60-fold enhancement of the electric field in the antenna gap. The simulations show that, with the help of the near-field scattering by the antenna, the optical trapping force on a 10 nm radius polystyrene nanoparticle is boosted by 3 orders of magnitude. A strong force acting on a nanoparticle located in the high-intensity region is observed when using a TE propagation mode in the waveguide to excite the antenna. The effects of the guided mode polarization on the force strength and trapping capability are also discussed in this paper. The novelty of this paper consists of using a trench waveguide that is capable of combining optofluidic and optical trapping in a single device and exploring mode polarization as a way to switch trapping.

The paper is organized as follows. Section 2 briefly introduces the Si_3N_4 trench waveguide fabrication and its optical performance. The design of a bow-tie antenna and the numerical characterization are also presented in this section. Section 3 shows the numerically simulated optical forces upon a polystyrene nanoparticle in two different states, lifting and flowing. The influence of the waveguide thickness, metal thickness, and guided mode polarization on the trapping force are also studied. A physically intuitive semi-analytical method to relieve the computation efforts and validate the full-wave simulations is presented in Section 4. The paper ends with a conclusion in Section 5, summarizing the performance and possible challenges in making the system practical.

2. WAVEGUIDE AND BOW-TIE ANTENNA DESIGN

A. Waveguide Design and Fabrication

Recently, we demonstrated a method to fabricate a sub-micrometer Si_3N_4 trench waveguide using conventional lithography, which has a low propagation loss of 0.8 dB/cm and high nonlinearity $n_2 = 1.39 \times 10^{-19}$ m^2/W [25,26]. Fabrication of this waveguide does not require E-beam lithography to achieve the sub-micrometer dimension but merely relies on optical lithography followed by anisotropic potassium hydroxide (KOH) etching. The KOH etching on a ⟨100⟩ silicon wafer carves a trapezoidal or triangular trench with an angle of 54.7° with respect to the substrate surface. The shape of the waveguide is determined by the etching depth D, the opening window W_{open}, and the Si_3N_4 deposition thickness T, as shown in Fig. 2(a). If W_{open} is smaller than $\sqrt{2}D$, a V-groove will be carved out, and the fabricated waveguide will be in a triangular shape. In contrast, if W_{open} is larger than that value, KOH will carve an isosceles trapezoidal trench. The width of the waveguide's lower edge can be estimated as $W_{btm} = W_{open} - \sqrt{2} \cdot D$. Low-pressure chemical vapor deposition is used to deposit a layer of a Si_3N_4 film with the thickness $T = 725 \pm 2.4$ nm.

The full-wave simulation result of a TE mode (electric field predominantly polarized along the x direction) in Fig. 2(b) shows that the mode can be confined in the trench region at 1550 nm. The simulation is performed with a finite element method (FEM) solver by COMSOL Multiphysics. Furthermore, we assume the refractive index of the Si_3N_4 to be $n_{Si_3N_4} = 2.14$, as measured in our earlier experimental work [25], whereas water and SiO_2 are assumed to have refractive indices $n_{H_2O} = 1.33$ and $n_{SiO_2} = 1.45$, respectively.

The mode field profile varies with the waveguide geometry. Wider waveguides favor TE modes, while narrow waveguides

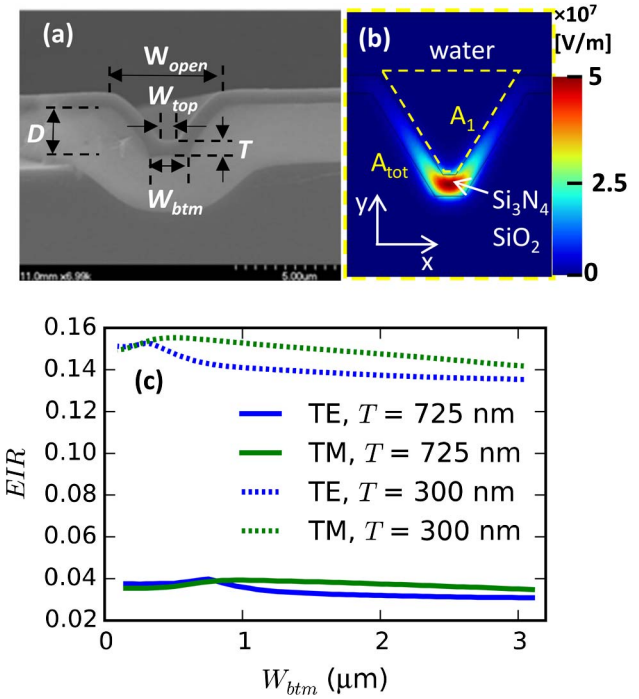

Fig. 2. (a) Scanning electron microscope image of a fabricated Si_3N_4 trench waveguide with the open width $W_{open} \approx 6.1$ μm as an example. (b) TE mode profile for the Si_3N_4 trench waveguide at 1550 nm with the parameters $W_{btm} = 1.15$ μm, $W_{top} = 500$ nm, $T = 725$ nm, and $D = 3.5$ μm. The electric field is mainly polarized in the x direction. (c) Evanescent intensity ratios (EIR) of the TE and TM modes as a function of W_{btm} and T.

better support TM modes (magnetic field is mainly along the x axis) [28]. It is worth mentioning that the TE mode is preferred for the plasmonic trapping applications because it will facilitate mode coupling from the waveguide to the bow-tie antenna that is aligned orthogonally to the waveguide direction (Fig. 1). Because the optical force is exerted by the gradient of the evanescent wave in the trench region, the evanescent intensity ratio (EIR) affects the trapping strength. The larger the EIR is, the stronger the light–matter interaction would be. The EIR is defined as in Eq. (1) [28]:

$$\mathrm{EIR} = \frac{\iint_{A_1} |E(x,y)|^2 \mathrm{d}x\mathrm{d}y}{\iint_{A_{\mathrm{tot}}} |E(x,y)|^2 \mathrm{d}x\mathrm{d}y}, \tag{1}$$

where A_1 is the cross-sectional area of the trapezoidal trench channel, and A_{tot} is the total simulation area that includes A_1, as shown in Fig. 2(b). In our case, A_{tot} is chosen to be 8 μm × 10 μm, which is large enough to include all the features of the electric field distributions. The fields outside the simulation region are negligible and thus can be safely disregarded. Here, we calculate the EIRs of the TE and the TM mode separately. The strength of the TE and the TM modes are mainly determined by the waveguide geometry. Figure 2(c) presents the EIRs of the TE and TM modes as a function of W_{btm} varying from 0.15 μm to 3.1 μm and $T = 300$ nm and 725 nm. For the waveguide with a thickness of 725 nm, if its W_{btm} is larger than 0.8 μm, then its fundamental mode is the TE mode; otherwise, for $W_{\mathrm{btm}} < 0.8$ μm, the fundamental mode will be the TM mode. For the waveguide with a thickness of 300 nm, the fundamental mode will be TM mode when $W_{\mathrm{btm}} < 0.44$ μm and be TE mode when $W_{\mathrm{btm}} \geq 0.44$ μm. The EIR of the TE mode in the $T = 725$ nm waveguide reaches its peak of 0.04 when $W_{\mathrm{btm}} = 0.75$ μm, while the maximum value in the $T = 300$ nm waveguide is 0.153 when $W_{\mathrm{btm}} = 0.3$ μm. The EIR of the TE mode is enhanced by 3.825 times when the waveguide thickness is thinned from 725 to 300 nm. The same is true for the EIRs of the TM modes. The EIR of the TM mode in the $T = 725$ nm waveguide has a peak value of 0.039 at $W_{\mathrm{btm}} = 1.0$ μm, while its peak value in the $T = 300$ nm waveguide is 0.155 at $W_{\mathrm{btm}} = 0.5$ μm. The EIR of the TM mode is enhanced by nearly four times when the waveguide is thinned from 725 to 300 nm. The degradation of EIR due to the waveguide width increment can be compensated by reducing the waveguide thickness. It is worth noting the effect of waveguide thickness on EIR is stronger than the effect of waveguide width. In our design, the width of W_{btm} is chosen to be 1.15 μm and, hence, the W_{top} to be 500 nm, which provides enough space in which to place a bow-tie antenna. The thickness parameter is adopted from the fabrication measurements and is 725 nm. The effects of the waveguide thickness on trapping force will be discussed in Section 3. With the chosen parameters, the EIR of the fundamental mode (the TE mode, which is chosen for its matched polarization, hence, for exciting the nanoantenna) for the trench waveguide is around 0.035. As a comparison, a rectangular strip waveguide with similar dimensions ($W_{\mathrm{btm}} = 1.15$ μm and $T = 725$ nm) has an EIR of 0.019 when calculated in the same sensing area A_1. It can be concluded that the trench waveguide under study has a stronger evanescent field in the region of interest than the regular strip waveguide with similar dimensions; thus, it is a better candidate for enabling light–matter interaction.

B. Nanoantenna Design

The optical gradient forces experienced by nanoparticles are typically very weak (some femtonewtons or less and limited by the power handling capability) because the dipolar polarizability scales with the third power of the particle size [29]. Therefore, to confine nanoparticles against destabilizing effects such as the thermal fluctuations, a significantly higher optical power is, in general, required. Fortunately, the plasmonic nature of metal nanostructures and the scattering effects of nanoantennas can enhance the electrical field intensity and its gradient, such that stable trapping can be achieved at a much lower power.

In recent years, bow-tie antenna arrays for particle manipulation in an objective lens configuration have been extensively studied [30]. When the incident light is linearly polarized across the gap of a bow-tie antenna, capacitive effects lead to a confined and intense electric field spot in the antenna near-field particularly within the gap. This hot spot increases the field intensity and significantly boosts the intensity gradient. A bow-tie antenna, made of two equilateral triangle gold patches separated by a gap along the x direction, can be deposited using nanosphere lithography [31,32]. The relative permittivity of the gold in this study is $\epsilon_{r,\mathrm{Au}} = -96.99 + i11.05$ at 1550 nm wavelength according to the Brendel–Bormann model [33].

As shown in Fig. 3(a), the electric field is greatly enhanced by the bow-tie antenna. The sharp peak represents the resonant field in the antenna gap, whereas the smoother peak around $y = 3$ μm represents the maximum of the electric modal field inside the waveguide. The field distributions are plotted along the y axis [Fig. 3(b)], and the origin is set to be at the bottom of the structure. The peak region circled in Fig. 3(a) is zoomed out in Fig. 3(c), illustrating the effect of the antenna length. The y position of the antenna top surface is denoted as the dashed line in Fig. 3(c). By manipulating the antenna length L shown in Fig. 3(e), the maximum electric field strength in the antenna gap can be altered, as shown in Fig. 3(d). We choose $L = 190$ nm in our design as an optimum value. Although a smaller gap leads to a stronger field, the gap of the bow-tie antenna is set to be 30 nm for the sake of particle trapping and relieving fabrication limitations. The sharpness of the antenna tip will also affect the field strength. A smaller radius of curvature R_1 will lead to a higher field enhancement. Considering fabrication imperfections, we assume R_1 and R_2 to be 10 nm. The apex angle θ will play a role in the field enhancement, too. However, we fix θ to be 30° for simplicity. The antenna thickness has been optimized to be 20 nm in order to maximize the optical trapping force, which will be discussed in Section 3. In the simulation of 10 mW launched power at 1550 nm wavelength, the peak intensity in the antenna gap (10 nm above the waveguide) can be 60 times larger than the case when there is no antenna at the same location.

3. OPTICAL TRAPPING PERFORMANCE

The optical trapping system to be studied is composed of a trench waveguide with $T = 725$ nm, $W_{\mathrm{btm}} = 1.15$ μm,

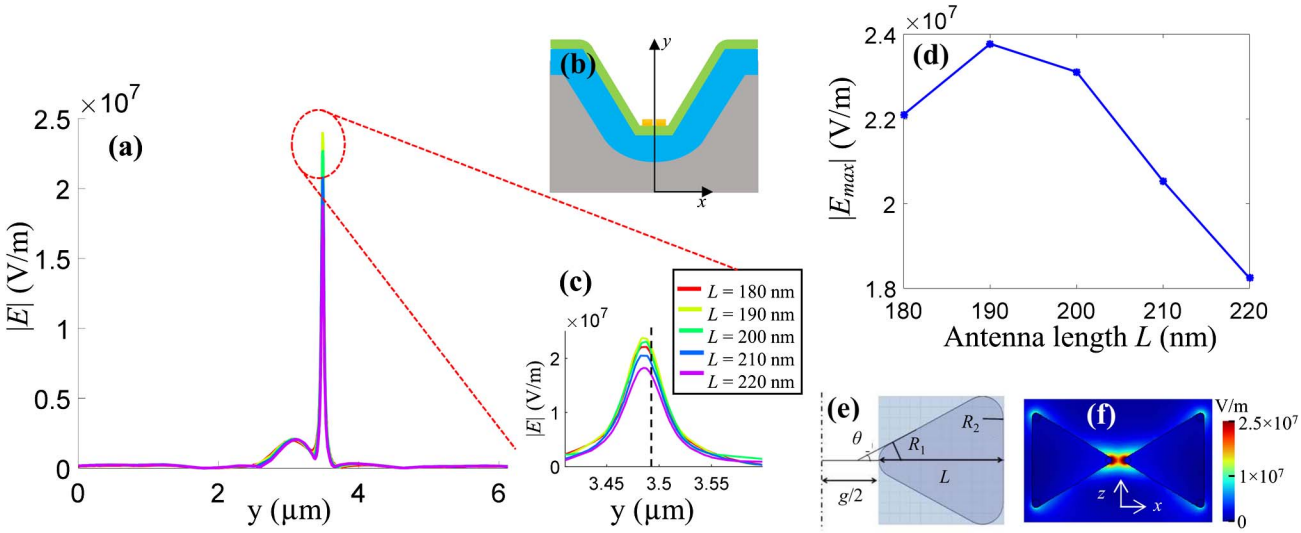

Fig. 3. (a) Electrical field profile along the y-oriented cutline (y axis) with different antenna lengths. The cutline is the y axis in (b). The circled region in (a) is zoomed out in (c). The black dashed line in (c) represents the y position corresponding to the antenna top surface. (d) The curve shows the maximum electric field with respect to different antenna lengths. (e) Half structure of a bow-tie antenna, with $g = 30$ nm, $R_1 = R_2 = 10$ nm, $\theta = 30°$ in our case. (f) Electric field profile at the top surface of the antenna, in the x–z plane.

and $D = 3.5$ μm and a bow-tie antenna with $L = 190$ nm, $g = 30$ nm, and $T_m = 20$ nm, where T_m is the metal thickness. The simulation results are obtained by using the built-in Maxwell stress tensor (MST) function in the RF module in the FEM-based solver COMSOL Multiphysics.

A polystyrene particle with a 10 nm radius immersed in water is placed in the proximity of the gap of a bow-tie plasmonic nanoantenna. The origin of y axis is set at the top surface of the bow-tie nanoantenna. The vertical distance from the particle's bottom to the bow-tie antenna top surface is denoted by H. Shown as the red curve in Fig. 4(a), the force direction is in the negative y direction; thus, it is a pulling force that can be used for optical trapping applications. Note that the force is proportional to the guided power in the waveguide. In the numerical analysis, we assume the waveguide to be excited by a TE mode with a power of 10 mW. The trapping force magnitude increases first when it is in the antenna gap, for increasing y, and then decreases as the nanoparticle is located farther away from the antenna. Without the antenna, the optical force caused by the gradient of evanescent wave decays exponentially as the particle lifts away from the waveguide, and it is orders of magnitude weaker than the one with the bow-tie nanoantenna. With the enhancement, the maximum force occurs when the particle bottom surface is 6 nm below the antenna top surface, right in the gap of antenna. At this position, the trapping force is boosted by 3 orders of magnitude compared with that occurring without antenna enhancement.

As discussed in Section 2.A, the thickness T of the waveguide affects EIR, which, in turn, influences optical forces. To quantify the influence, we compare the vertical trapping forces magnitude $|F_y|$ upon the same polystyrene particle on two different waveguides with different thicknesses, as shown in Fig. 4(b). $|F_y|$ is boosted nearly three times, as the waveguide thickness shrinks from 725 to 300 nm. The result agrees with the aforementioned EIR study that higher EIR leads to stronger light–matter interaction. The maximum force is 33 pN/W for our 300 nm thick waveguide, which is close to the value reported in [14] with the same antenna gap $g = 30$ and particle diameter 20 nm but a thinner waveguide $h = 250$ nm. We conclude that reducing our waveguide thickness will further improve the trapping force strength, and the results will be superior to previous work.

The effect of antenna thickness on the vertical trapping force has also been studied, and the results are illustrated in Fig. 4(c). The origin of the y axis is set to be the top surface of each antenna, and H is counted from the particle bottom surface with respect to the origin. We simulate the cases when the particle is in the gaps of the antennas that have three different thicknesses: 20, 30, and 40 nm. All the maxima occur when the particle bottom surface is around 6 nm below the antenna top surface. A thinner antenna gives stronger force magnitude. The comparison verifies that 20 nm metal thickness will facilitate optical trapping in our design. For given parameters, we find that there is a net gradient force that is always in the $-y$ direction for antenna thicknesses <30 nm, which is pulling the particle toward the waveguide surface. There is no force repelling the particle away from the waveguide. The buoyant force is smaller than the particle gravity for the polystyrene beads. Hence, it is safe to assume that the particle will be trapped at the waveguide surface. However, for a thick bow-tie antenna [≥30 nm in Fig. 4(c)], there will be a net gradient force in $+y$ direction as the particle gets closer to the waveguide surface. Thus, the particle may not be trapped on the waveguide surface.

Besides particle trapping in the vertical direction, the scenarios of a flowing nanoparticle passing by the antenna gap are also studied. It is assumed that the nanoparticle keeps the same height, 5 nm above the nanoantenna top surface ($H = 5$ nm), during its movement in the z and x directions. Five situations are considered, as shown in Fig. 5(a): the nanoparticle passing

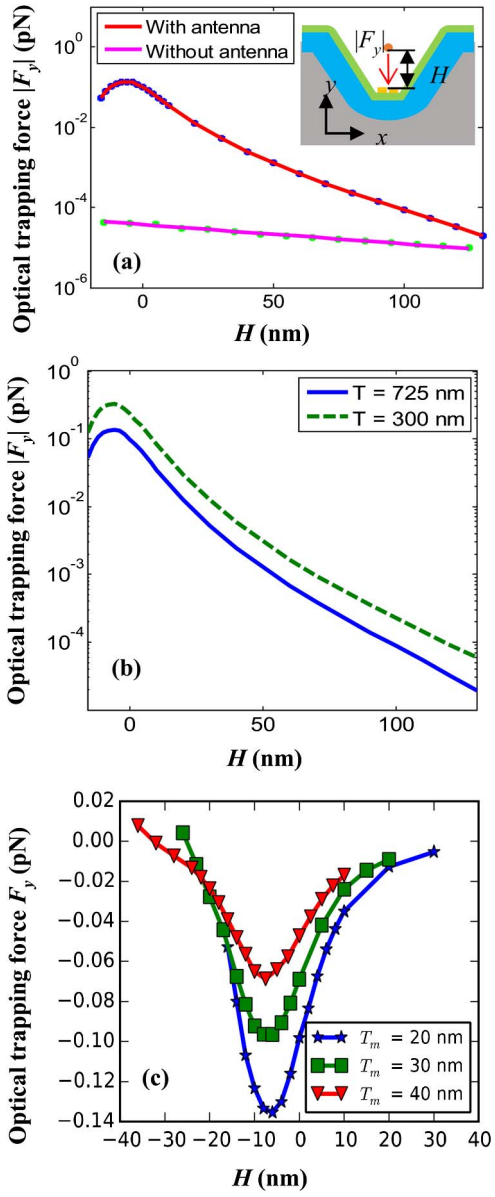

Fig. 4. (a) Magnitude of the downward optical trapping force along the negative y direction versus vertical distance H from the particle bottom surface to the antenna top surface. The force enhanced by the bow-tie antenna is compared with the one without bow-tie antenna, showing orders of magnitude force increase. (b) Magnitude of the vertical trapping force as a function of H and T. (c) Effect of the antenna thickness on the vertical trapping forces: T_m stands for the bow-tie metal thickness. The origin of the y axis is set to be at the top surface of each antenna, and H is counted from the base of the particle to the origin. The results presented in (a) and (c) are generated for the trench waveguide with $T = 725$ nm, $W_{\text{top}} = 500$ nm, and $W_{\text{btm}} = 1.15$ μm. The results in (b) are generated for the waveguides with $W_{\text{top}} = 500$ nm and $T = 725$ nm and 300 nm.

along a trajectory coinciding with the z axis, along the antenna center ($x = 0$); the particle passing near the symmetric axis of the antenna ($x = 10$, $x = 30$ nm, and $x = 50$ nm); the particle passing along the x axis. The optical force components in the x, y and z directions are computed numerically and curve-fitted as the nanoparticle moves along the trajectories, as shown in Figs. 5(b)–5(f).

When the nanoparticle flows along the z axis ($x = 0$), as shown in Fig. 5(b), the vertical optical force F_y remains negative, indicating the force is pulling the particle downward. The longitudinal force F_z changes its sign corresponding to the particle position. In particular, when z is positive, F_z is negative, and vice versa, which means the optical force F_z tends to attract the nanoparticle back when it moves away from the antenna center. The maximum F_z occurs when the particle is 10 nm away from the center. The horizontal force F_x is negligible compared with the other two components, and it is expected to be zero ideally because of symmetry reasons. Ripples in F_x may arise from numerical errors due to finite mesh size and nonsymmetrical mesh. The force profiles in the case when $x =$ 10 nm [Fig. 5(c)] are similar to the case when $x = 0$, except that F_x becomes significant compared with the other force components. F_x is initially positive when x is positive, meaning that the force repels the particle away from the antenna gap in the $+x$ direction. When the particle is farther away from the antenna center, i.e., $x = 30$ nm, as shown in Fig. 5(d), F_y and F_z become weaker. However, F_x changes its sign. F_x becomes negative when x is positive, indicating that the force pulls the particle toward the antenna gap in the $-x$ direction. When the particle is even farther away from the antenna gap, i.e., $x = 50$ nm, as shown in Fig. 5(e), the force profiles resemble those in Fig. 5(d) but have smaller magnitudes. The opposite F_x force profiles in Figs. 5(c) and 5(d) imply that the particle might be trapped at the antenna tips. To further investigate the trapping locations, we simulate the case when the particle position is swept along the x axis ($z = 0$). As shown in Fig. 5(f), F_x changes its sign, and F_y reaches the maximum magnitude at $x = 15$ nm. F_z remains close to zero during the movement due to symmetry of the structure and the subwavelength size of the nanoantenna. The profiles indicate that the nanoparticle will be trapped to the antenna tips because the antenna tips in our design are located at $x = \pm 15$ nm. The results are reasonable because the gradient force tends to drive the particle toward the highest-intensity region if the particle is optically denser than the surrounding medium. Therefore, the particles will be trapped to the antenna tips. This conclusion also can be confirmed by the intensity profile of the antenna, as shown in Fig. 3(f).

The aforementioned optical forces are generated by the antenna scattering excited by a propagating TE mode in the waveguide. We also investigated the optical trapping force generated by a TM mode propagating in the same waveguide. The vertical forces caused by different propagation modes near the antenna region are compared and illustrated in Fig. 6(a). The simulation mainly covers the case when the particle falls into the antenna gap, i.e., for H ranging from −15 to 8 nm, where the trapping force is the strongest. The vertical force F_y generated by the TE wave is at least 2 orders of magnitude larger than that generated by the TM wave. Here, we recall that the bow-tie nanoantenna orientation is set to match with the electric field of the TE mode, whereas the TM mode fails to excite the nanoantenna leading to much weaker scattering and near field. The longitudinal force F_z is also simulated

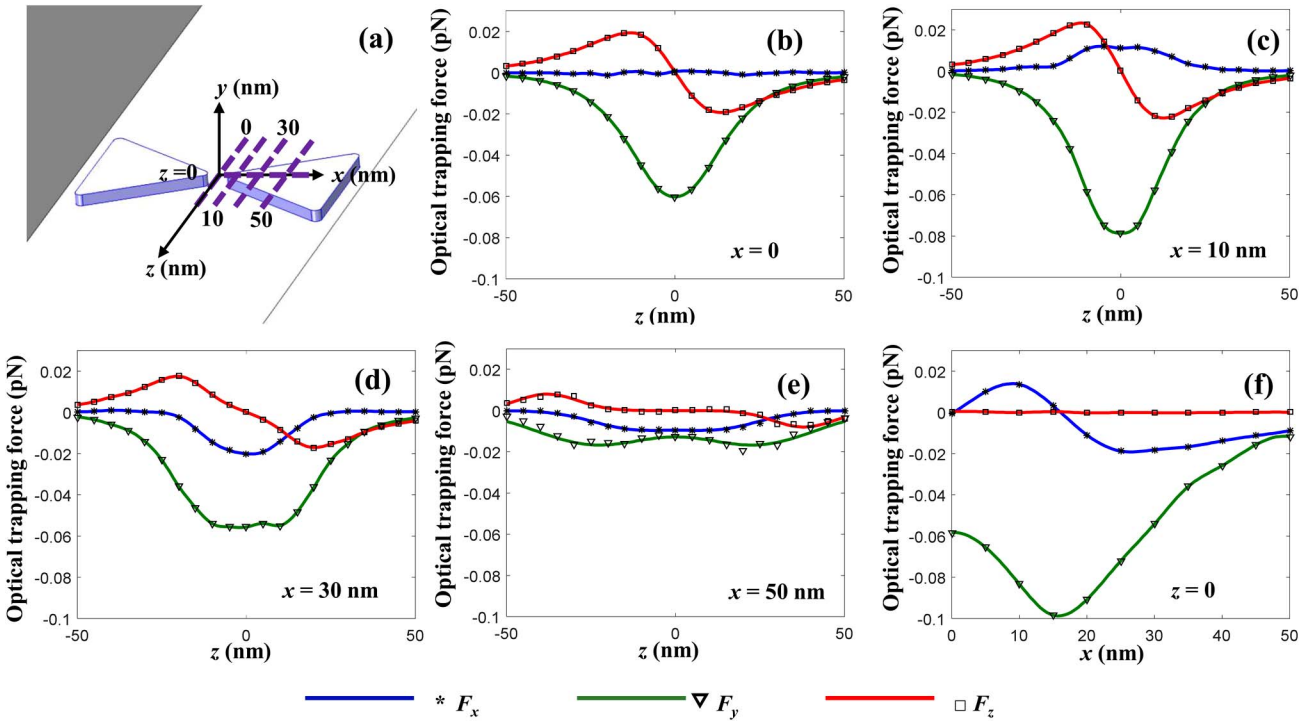

Fig. 5. Simulation of the optical trapping forces on a nanoparticle flowing in the z direction and the x direction with 10 mW input power. (a) The nanoparticle moves along the dashed z-oriented lines from $z = -50$ nm to $z = 50$ nm and the dashed x-oriented line from $x = 0$ to $x = 50$ nm. The four z-oriented dashed lines represent the cases when the particle is in the center ($x = 0$) and away from the antenna central symmetric axis ($x = 10$ nm, $x = 30$ nm, and $x = 50$ nm). The x-oriented dashed line represents the case when the particle moves along the x axis ($z = 0$). The vertical distance H is kept the same in all cases, with the nanoparticle bottom surface 5 nm above the antenna top surface ($H = 5$ nm). Optical trapping force components upon the nanoparticle when $x = 0$ (b), $x = 10$ nm (c), $x = 30$ nm (d), $x = 50$ nm (e), and $z = 0$ (f).

in Fig. 6(b) by moving the particle along the centerline of the antenna along the z direction, while keeping the same height $H = -6$ nm. Compared with the TE mode, the longitudinal force F_z in the TM mode is negligible. Importantly, the force F_z has the same sign as position z, indicating it is a repelling force and loses the trapping functionality. Thereby, the mode polarization severely affects the trapping functionality. In general, the TE mode is used for optical trapping, while switching to TM mode can help release the particle from the antenna.

4. SEMI-ANALYTICAL CALCULATION

The optical trapping force, presented in Section 3, is simulated by an FEM solver using the MST method. To simulate the optical force at each particle position, the software has to solve the mode distribution and integrate the Maxwell stress tensor, which takes tremendous computing resources to simulate the nanostructures in a micro-size model. An analytical method is discussed here to relieve the computation efforts by extracting the field distributions from a one-time full-wave simulation and calculating the optical force relying on the extracted fields. For optical trapping in the Rayleigh regime, i.e., when the particle size is much smaller than the wavelength, a dipole approximation can be used to analytically describe the force upon the particle [34,35]. The induced dipole polarizability influences the interaction strength with an optical field. For a sphere of radius a and relative electric permittivity ϵ_{r1}, using SI units, the point-like particle polarizability α_0 is approximately given by the Clausius–Mossotti relation [34]:

$$\alpha_0 = 4\pi\epsilon_0\epsilon_{r2}a^3\frac{\epsilon_{r1}-\epsilon_{r2}}{\epsilon_{r1}+2\epsilon_{r2}}, \tag{2}$$

where $\epsilon_{r1} = 2.46$ is the polystyrene nanoparticle's relative permittivity, $\epsilon_{r2} = 1.77$ is the host medium relative permittivity, and ϵ_0 is the vacuum permittivity. If taking the reaction of a finite-size dipole to the scattered field at its own location into consideration, i.e., accounting for radiation losses, the Clausius–Mossotti relation can be corrected as follows [35]:

$$\alpha = \frac{\alpha_0}{1-\frac{ik_2^3\alpha_0}{6\pi\epsilon_{r2}\epsilon_0}}, \tag{3}$$

where k_2 is the wavenumber in the host medium.

The explicit form of the time-averaged force acting on such a dipole is in [35]:

$$\langle\mathbf{F}\rangle = \frac{1}{4}\mathrm{Re}(\alpha)\nabla|\mathbf{E}|^2 + \frac{\sigma}{2c}\mathrm{Re}(\mathbf{E}\times\mathbf{H}^*) + \frac{\sigma c\epsilon_2}{4\omega i}\nabla\times(\mathbf{E}\times\mathbf{E}^*), \tag{4}$$

where the total (or extinction) cross section of the particle $\sigma = k_2\,\mathrm{Im}\{\alpha\}/\epsilon_2$ [36]. The first term in the right-hand side of the equation is the optical gradient force, the second term represents radiation pressure, and the third one is the polarization gradient force. The particle cross section σ scales with

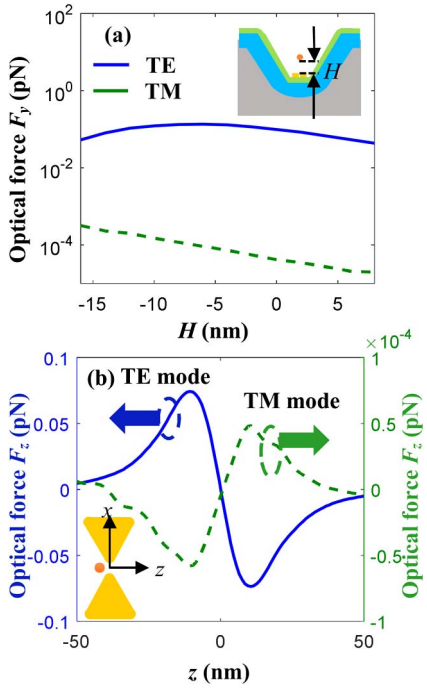

Fig. 6. (a) Magnitude of vertical optical forces F_y generated by the TE and TM propagation modes in the Si_3N_4 waveguide with $W_{top} = 500$ nm and $T = 725$ nm. The particle is at the antenna center in the x–z plane but moves vertically from $H = -15$ nm to $H = 8$ nm. (b) The longitudinal optical force F_z generated by the TE and TM propagation modes in the same waveguide. The particle remains the same height $H = -6$ nm and flows along the centerline of the antenna from $z = -50$ nm to $z = 50$ nm. The input power is 10 mW.

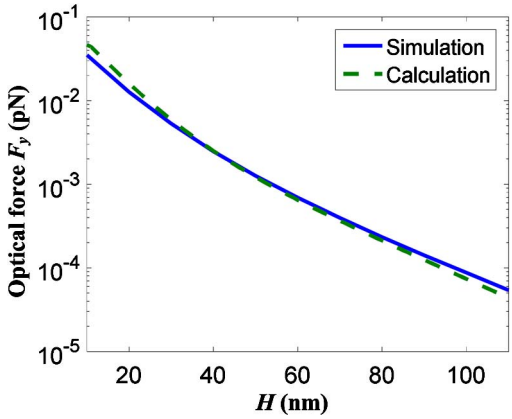

Fig. 7. Comparison of force computations. The analytic optical force is evaluated based on Eq. (5) and compared with the total force simulated by using a FEM-based full-wave method combined with a Maxwell stress tensor method.

a^6 (a is particle radius) when the particle size is smaller than the wavelength [37]; thus, the magnitude of the radiation pressure and polarization gradient force is several orders smaller than the optical gradient force and can be neglected. Given that the particle size is sufficiently small ($a = 10$ nm) compared with the wavelength (1550 nm), perturbation theory can be applied such that the field experienced by the nanoparticle can be calculated from the evanescent fields in the cladding without the existence of the particle. In addition, we do not consider the case where the particle falls into the antenna gap to avoid self-induced back-action [38]. Thus, the electric field experienced by the nanoparticle is approximately represented by the scattering field of the antenna itself [36]. We scrutinize the vertical optical force F_y in the region where the polystyrene sphere is lifted from $H = 10$ nm to $H = 110$ nm (we recall H is the distance from the bow-tie top surface to the bottom of the nanoparticle). Thereby, by retaining only the first term of the Eq. (4), it can be written in the following way in favor of calculating F_y:

$$\langle F_y \rangle \approx \frac{1}{4}\,\mathrm{Re}(\alpha)\,\frac{\partial}{\partial y}\left(|E_x|^2 + |E_y|^2 + |E_z|^2\right). \tag{5}$$

In data processing, we extract the electric fields in the cladding for simplicity and calculate the fields experienced by the nanoparticle using the electric displacement continuity equation. To reduce the noise effect that comes from numerical errors, the data are fitted by exponential curves. We calculate the optical trapping force in the y direction and compare it with the previous full-wave results obtained by using the MST method in COMSOL, as shown in Fig. 7. The calculated optical gradient force well matches the full-wave simulated force. Both methods (full-wave and semi-analytical) are in agreement at all locations. Despite a small discrepancy, which may result from imperfect curve fitting, the trend versus distance is the same, and the results show consistency. The semi-analytical method used in this section is not limited to trench waveguides and can be applied to other waveguide-based trapping systems as well. It provides a fast approach for estimating optical forces on particles in the Rayleigh regime. Instead of solving for the field distribution and calculating the optical force at every particle position, one can extract the field distribution from a simulation and use it to calculate the force gradient and thus the optical force. The limitation of the approach, however, is that the presence of the particle should behave as a small perturbation to the local fields and not significantly perturb the field distribution.

5. CONCLUSION

We have demonstrated the trapping capability of a plasmonic bow-tie nanoantenna patterned on a Si_3N_4 trench optical waveguide. The simulated force on a polystyrene nanoparticle was boosted by 3 orders of magnitude with the help of the nanoantenna. The polarization dependency of the trapping force equipped the device with switching capabilities. The force was also analytically verified and shown to be in agreement with the full-wave simulation results. This investigation indicates that a nanostructure patterned Si_3N_4 waveguide is suitable for optical trapping and nanoparticle sensing applications. To further increase the trapping capability of the system, we suggested using a thinner waveguide to enhance the light–matter interaction. Meanwhile, adding more antennas along the waveguide axis can also increase nanoparticle capture chances.

The main challenge in this design is how to fabricate an antenna in the trench waveguide. However, the fabrication

difficulties should not dim the novelty of the design, which combines optofluidic and optical trapping in a single device and also puts forward using mode polarization optical trapping switching. Moreover, trench waveguides are not limited to the proposed structure but can be tailored to be compatible with current fabrication technique. As stated in Section 2.A, we can use wider but shallow waveguides, so that the trench base width will be wide enough for nanosphere lithography. Hence, the research method can be applied to other waveguides and nanoantennas. In particular, any nanoantennas based on colloidal nanoparticles [39] can be used to create local hot spots on the trench waveguides to perform optical trapping.

Funding. National Science Foundation (NSF) (SNM ECCS 1449397).

REFERENCES

1. A. Ashkin, "Acceleration and trapping of particles by radiation pressure," Phys. Rev. Lett. **24**, 156–159 (1970).
2. D. G. Grier, "A revolution in optical manipulation," Nature **424**, 810–816 (2003).
3. M. P. MacDonald, G. C. Spalding, and K. Dholakia, "Microfluidic sorting in an optical lattice," Nature **426**, 421–424 (2003).
4. A. N. Grigorenko, N. W. Roberts, M. R. Dickinson, and Y. Zhang, "Nanometric optical tweezers based on nanostructured substrates," Nat. Photonics **2**, 365–370 (2008).
5. A. Ashkin, J. M. Dziedzic, J. E. Bjorkholm, and S. Chu, "Observation of a single-beam gradient force optical trap for dielectric particles," Opt. Lett. **11**, 288–290 (1986).
6. R. Dasgupta, S. Ahlawat, P. K. Gupta, J. Xavier, and J. Joseph, "Optical trapping with low numerical aperture objective lens," in *Photonics Global Conference (PGC)* (2012), pp. 1–4.
7. R. Dasgupta, S. Ahlawat, and P. K. Gupta, "Trapping of micron-sized objects at a liquid-air interface," J. Opt. Pure Appl. Opt. **9**, S189–S195 (2007).
8. Y. Harada and T. Asakura, "Radiation forces on a dielectric sphere in the Rayleigh scattering regime," Opt. Commun. **124**, 529–541 (1996).
9. A. H. J. Yang, S. D. Moore, B. S. Schmidt, M. Klug, M. Lipson, and D. Erickson, "Optical manipulation of nanoparticles and biomolecules in sub-wavelength slot waveguides," Nature **457**, 71–75 (2009).
10. D. Erickson, X. Serey, Y.-F. Chen, and S. Mandal, "Nanomanipulation using near field photonics," Lab. Chip **11**, 995–1009 (2011).
11. M. Soltani, J. Lin, R. A. Forties, J. T. Inman, S. N. Saraf, R. M. Fulbright, M. Lipson, and M. D. Wang, "Nanophotonic trapping for precise manipulation of biomolecular arrays," Nat. Nanotechnol. **9**, 448–452 (2014).
12. S. Kühn, P. Measor, E. J. Lunt, B. S. Phillips, D. W. Deamer, A. R. Hawkins, and H. Schmidt, "Loss-based optical trap for on-chip particle analysis," Lab Chip **9**, 2212–2216 (2009).
13. M. L. Juan, M. Righini, and R. Quidant, "Plasmon nano-optical tweezers," Nat. Photonics **5**, 349–356 (2011).
14. P.-T. Lin, H.-Y. Chu, T.-W. Lu, and P.-T. Lee, "Trapping particles using waveguide-coupled gold bow-tie plasmonic tweezers," Lab Chip **14**, 4647–4652 (2014).
15. W. Zhang, L. Huang, C. Santschi, and O. J. F. Martin, "Trapping and sensing 10 nm metal nanoparticles using plasmonic dipole antennas," Nano Lett. **10**, 1006–1011 (2010).
16. M. Righini, P. Ghenuche, S. Cherukulappurath, V. Myroshnychenko, F. J. García de Abajo, and R. Quidant, "Nano-optical trapping of rayleigh particles and escherichia coli bacteria with resonant optical antennas," Nano Lett. **9**, 3387–3391 (2009).
17. P. Hansen, Y. Zheng, J. Ryan, and L. Hesselink, "Nano-optical conveyor belt, Part I: theory," Nano Lett. **14**, 2965–2970 (2014).
18. Y. Zheng, J. Ryan, P. Hansen, Y.-T. Cheng, T.-J. Lu, and L. Hesselink, "Nano-optical conveyor belt, Part II: demonstration of handoff between near-field optical traps," Nano Lett. **14**, 2971–2976 (2014).
19. G. Wang, Z. Ying, H. Ho, Y. Huang, N. Zou, and X. Zhang, "Nano-optical conveyor belt with waveguide-coupled excitation," Opt. Lett. **41**, 528–531 (2016).
20. B. S. Schmidt, A. H. Yang, D. Erickson, and M. Lipson, "Optofluidic trapping and transport on solid core waveguides within a microfluidic device," Opt. Express **15**, 14322 (2007).
21. S. Mandal and D. Erickson, "Optofluidic transport in liquid core waveguiding structures," Appl. Phys. Lett. **90**, 184103 (2007).
22. X. Fan and I. M. White, "Optofluidic microsystems for chemical and biological analysis," Nat. Photonics **5**, 591–597 (2011).
23. M. Chamanzar, Z. Xia, S. Yegnanarayanan, and A. Adibi, "Hybrid integrated plasmonic-photonic waveguides for on-chip localized surface plasmon resonance (LSPR) sensing and spectroscopy," Opt. Express **21**, 32086 (2013).
24. Y. Luo, M. Chamanzar, A. Apuzzo, R. Salas-Montiel, K. N. Nguyen, S. Blaize, and A. Adibi, "On-chip Hybrid photonic-plasmonic light concentrator for nanofocusing in an integrated silicon photonics platform," Nano Lett. **15**, 849–856 (2015).
25. Y. Huang, Q. Zhao, L. Kamyab, A. Rostami, F. Capolino, and O. Boyraz, "Sub-micron silicon nitride waveguide fabrication using conventional optical lithography," Opt. Express **23**, 6780–6786 (2015).
26. Y. Huang, Q. Zhao, N. Sharac, R. Ragan, and O. Boyraz, "Highly nonlinear sub-micro silicon nitride trench waveguide coated with gold nanoparticles," Proc. SPIE **9503**, 95030H (2015).
27. Q. Zhao, C. Guclu, Y. Huang, F. Capolino, and O. Boyraz, "Plasmon optical trapping in silicon nitride trench waveguide," in *CLEO* (OSA, 2015), paper JTu5A.80.
28. Q. Zhao, Y. Huang, R. Torun, S. Rahman, T. C. Atasever, and O. Boyraz, "Numerical investigation of silicon nitride trench waveguide," Proc. SPIE **9586**, 95860O (2015).
29. W. H. Wright, G. J. Sonek, and M. W. Berns, "Radiation trapping forces on microspheres with optical tweezers," Appl. Phys. Lett. **63**, 715–717 (1993).
30. B. J. Roxworthy, K. D. Ko, A. Kumar, K. H. Fung, E. K. C. Chow, G. L. Liu, N. X. Fang, and K. C. Toussaint, "Application of plasmonic bow-tie nanoantenna arrays for optical trapping, stacking, and sorting," Nano Lett. **12**, 796–801 (2012).
31. T. R. Jensen, M. D. Malinsky, C. L. Haynes, and R. P. Van Duyne, "Nanosphere lithography: tunable localized surface plasmon resonance spectra of silver nanoparticles," J. Phys. Chem. B **104**, 10549–10556 (2000).
32. A. J. Haes, C. L. Haynes, A. D. McFarland, G. C. Schatz, R. P. Van Duyne, and S. Zou, "Plasmonic materials for surface-enhanced sensing and spectroscopy," MRS Bull. **30**, 368–375 (2005).
33. A. D. Rakic, A. B. Djurišic, J. M. Elazar, and M. L. Majewski, "Optical properties of metallic films for vertical-cavity optoelectronic devices," Appl. Opt. **37**, 5271–5283 (1998).
34. B. T. Draine, "The discrete-dipole approximation and its application to interstellar graphite grains," Astrophys. J. **333**, 848–872 (1988).
35. O. M. Maragò, P. H. Jones, P. G. Gucciardi, G. Volpe, and A. C. Ferrari, "Optical trapping and manipulation of nanostructures," Nat. Nanotechnol. **8**, 807–819 (2013).
36. S. Albaladejo, M. I. Marqués, M. Laroche, and J. J. Sáenz, "Scattering forces from the curl of the spin angular momentum of a light field," Phys. Rev. Lett. **102**, 113602 (2009).
37. A. J. Cox, A. J. DeWeerd, and J. Linden, "An experiment to measure Mie and Rayleigh total scattering cross sections," Am. J. Phys. **70**, 620–625 (2002).
38. M. L. Juan, R. Gordon, Y. Pang, F. Eftekhari, and R. Quidant, "Self-induced back-action optical trapping of dielectric nanoparticles," Nat. Phys. **5**, 915–919 (2009).
39. S. M. Adams, S. Campione, J. D. Caldwell, F. J. Bezares, J. C. Culbertson, F. Capolino, and R. Ragan, "Non-lithographic SERS substrates: tailoring surface chemistry for Au nanoparticle cluster assembly," Small **8**, 2239–2249 (2012).